Science Advances

AAAS

Supplementary Materials for

Super-resolution nanoscopy by coherent control on nanoparticle emission

Congyue Liu, Wei Liu, Shufeng Wang*, Hongjia Li, Zhilong Lv, Fa Zhang*, Donghui Zhang, Junlin Teng, Tao Zheng,
Donghai Li, Mingshu Zhang, Pingyong Xu, Qihuang Gong*

*Corresponding author. Email: wangsf@pku.edu.cn (S.W.); zhangfa@ict.ac.cn (F.Z.); qhgong@pku.edu.cn (Q.G.)

This PDF file includes:

Supplementary Text
Figs. S1 to S10

Supplementary Text

　　Femtosecond laser pulses are broad-spectrum sources that are compressed into a limited pulse in time and contain many continuous frequency components. The pulse shaping technique is to modify the pulse shape, spatial polarization, amplitude, and phase. This method described in this paper is based on time-invariant filter, which is a well-known concept in electronic engineering.

　　The expression of pulse shaping process in time domain can be expressed simply by Fourier transform. In the time domain, the filter is described by pulse response function $h(t)$. The output field of the filter $e_{out}(t)$ in response to an input pulse $e_{in}(t)$ is given by the convolution of $e_{in}(t)$ and $h(t)$.

$$e_{out}(t) = e_{in}(t) * h(t) = \int d\tau\, e_{in}(\tau) h(t-\tau)$$

　　In the frequency domain, the filter is described by pulse response function $H(\omega)$. The output field $E_{out}(\omega)$ from the filter can be expressed by the product of the input field $E_{in}(\omega)$ and the response function $H(\omega)$.

$$E_{out}(\omega) = E_{in}(\omega) \cdot H(\omega)$$

　　The above $e_{in}(t)$ & $E_{in}(\omega)$, $e_{out}(t)$ & $E_{out}(\omega)$ and $h(t)$ & $H(\omega)$ are Fourier transform pairs. The process of pulse shaping is to calculate the input field $E_{in}(\omega)$ and filter $H(\omega)$ in frequency domain by Fourier transform, and multiply them to get the frequency domain expression of the output field $E_{out}(\omega)$, and get the time expression of the output $e_{out}(t)$ by inverse transform, which is shown as below:

$$e_{out}(t) = \frac{1}{2\pi} \int E_{out}(\omega) \cdot e^{i\omega t}\, d\omega$$

　　According to these relations, when the input field $e_{in}(t) = \delta(t)$, the field in the frequency domain $E_{in}(\omega) = 1$. This means that the output field $E_{out}(\omega)$ is equal to the filter response function $H(\omega)$. It is shown that the desired shaping of pulses can be achieved by making specific filters. This is also the foundation of pulse shaping.

　　Usually, we add a modulator in the frequency domain of the system, that is, the response function $H(\omega)$.

$$H(\omega) = \frac{E_{out}(\omega)}{E_{in}(\omega)} = \frac{A(\omega)e^{i\emptyset_{out}(\omega)}}{A_{in}(\omega)e^{i\emptyset_{in}(\omega)}} = T(\omega) \cdot e^{i\Delta\emptyset(\omega)}$$

　　Where $T(\omega)$ is amplitude modulation (AM) function, $e^{i\Delta\emptyset(\omega)}$ is phase modulation (PM) function.

　　For known input pulses, a variety of modulation functions can generate new pulse shapes. Some basic responses are as Fig. S1B.

　　By Fourier transform, pulses are converted into double pulses, pulse trains, pulse broadening, chirp signals, etc. For more complex shaped pulse generated, it can be achieved by designing more complex modulation functions.

　　Pulse shaping is not only controlling the amplitude and phase of the femtosecond pulse, but also the polarization characteristics. In the experiment, the spatial light modulator is actually a one-dimensional array of liquid crystal pixels with two-layer structure. Each layer can be controlled separately. The (molecular alignment) axis angles between the liquid crystal of two layers is 90°, and they are +45°and -45° to the laser polarization. So the two liquid crystal layers

work as two tunable waveplates with axis perpendicular to each other. The initial linear polarization of the pulse will become elliptical polarization after passing through the first "waveplate". With arbitrary voltage applied, the polarization ellipticity could be controlled. E.g., with proper applied voltages, the "waveplate" could be $1/4\lambda$ or $1/2\lambda$ plates, which changes the initial linear polarization to circular polarization or linear one perpendicular to the original polarization, respectively. Since the two layer of modulators have their axis perpendicular to each other, they could compensate each other if same voltage applied. However, with different voltage applied, the final output polarization could be effectively controlled. It should be noticed that since the two axis are fixed in space, the output polarizations are not supposed to be linear with arbitrary orientation - for most of the cases, the output is an elliptically polarized light pulse. However, since this study ask for the random polarization instead of any specified one, this polarization manipulation is effective for the control.

Because of the dispersion with the grating, different frequencies are separated in space and sent into different pixel units. Each pixel can manipulate the phase and polarization characteristics of the laser pulse. After passing through the conjugated grating, the separated frequency component re-combined into a new femtosecond pulse with complex phase and polarization.
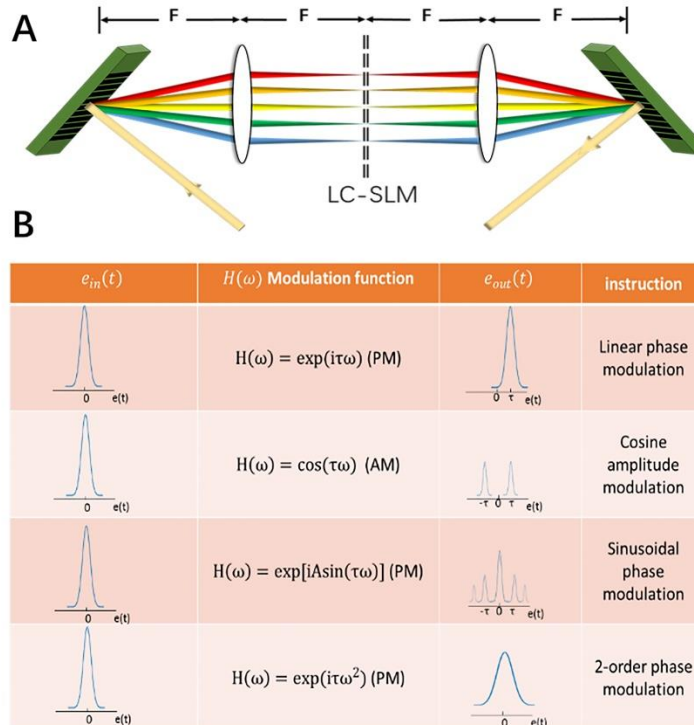
A

LC–SLM

B

$e_{in}(t)$	$H(\omega)$ **Modulation function**	$e_{out}(t)$	instruction
	$H(\omega) = \exp(i\tau\omega)$ (PM)		Linear phase modulation
	$H(\omega) = \cos(\tau\omega)$ (AM)		Cosine amplitude modulation
	$H(\omega) = \exp[iA\sin(\tau\omega)]$ (PM)		Sinusoidal phase modulation
	$H(\omega) = \exp(i\tau\omega^2)$ (PM)		2-order phase modulation

Fig. S1. The demonstration of pulse shaper. (A) The pulse shaper system is composed of a 4F system mainly. The femtosecond laser beam centers at 800nm, with pulse width ~7fs (Rainbow, Femtolasers). The wavelengths between 750-850nm are used by the shaper system. The laser pulse is split into frequency domain by a grating firstly. The dispersed beams with are then focused onto a double layer, multi-element 1-D liquid crystal spatial light modulator (640D, Jenoptik) through a cylindrical lens. The birefringence refractive index of each element is independently programmable. Therefore, the phase and polarization of each wavelength can be tuned independently. By collimating and then combining through a second grating, a shaped pulse is generated, with modulated temporal characteristics of phase, amplitude, and polarization. For different sample systems, the initial setting of pulse shaper should be the optimal pulse for fluorescence yield. We usually apply adaptive genetic algorithm to obtain the optimal phase pulse. On the basis of the optimal pulse, the shaping pulse can be obtained by adding a small random phase to each pixel unit of the liquid crystal array, since we believe that the modulation effect near the optimal phase is the most sensitive. **(B)** Common examples of pulse shaping. The shaping results of a limit pulse through different modulation functions of a pulse shaper could be obtained. Pulses are converted into double pulses, pulse trains, pulse broadening, chirp signals, etc. Similarly, more complex modulation functions can be designed to generate complex shaping pulses corresponding to expectations.
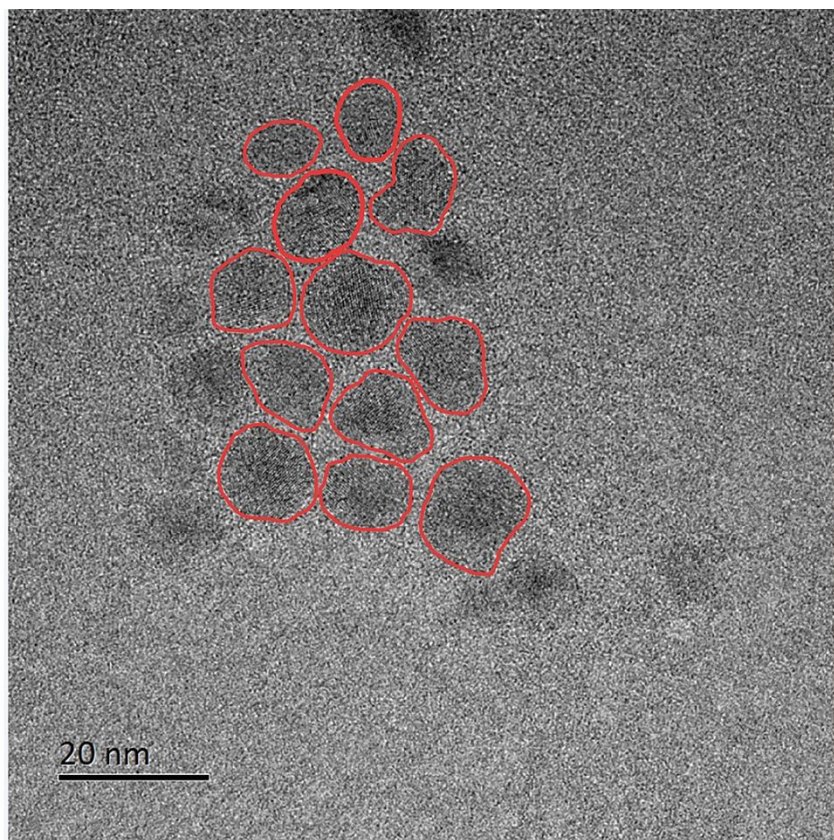
Fig. S2. Transmission electron microscopy(TEM) image of ZnCdS quantum dots. Although quantum dots can be regarded as identical particles, their shape, size, crystal phase, and defects are still slightly different (circled by red lines).
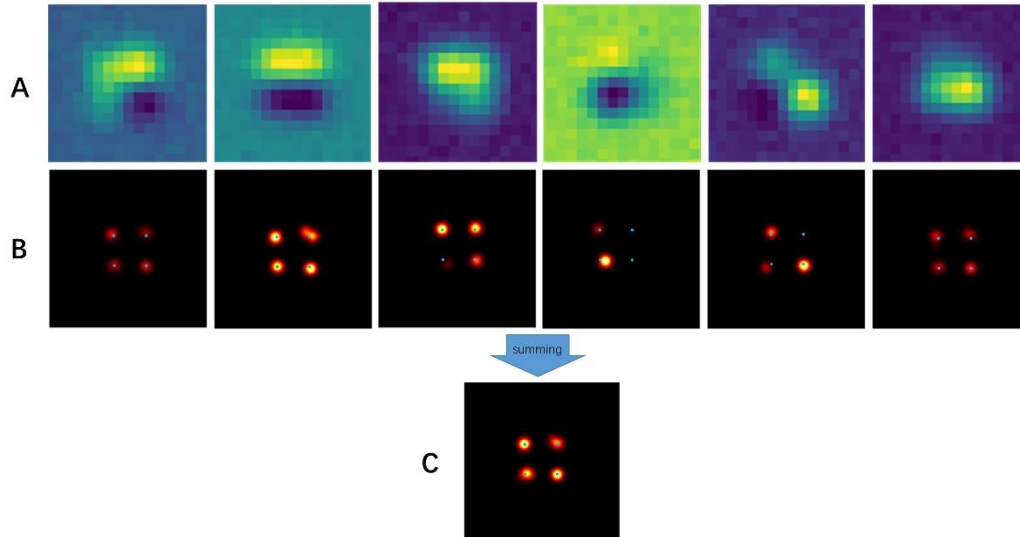
Fig. S3. Demonstration of Combination FFT imaging process to reduce localization errors. The purpose is to express the super-resolution results that breakthrough the diffraction limit through a whole set of experiments and data processing schemes in Fig.2 of the article. The summing process conforms to the statistical law and reduces the random error of the result of each one frame, as following figure. **(A)** The first line is a preprocessed image of four emitters after combination FFT process. **(B)** After Multi-Gauss fitting of each frame's preprocessed image, the corresponding location results are obtained in the second line. The four blue points in each result of **B** represent the original true position of the emitters. It can be seen that there is still a large visible localization error between analytical result and the real position of each image. This is usually happened when resolved spots present large brightness difference. Therefore, by multiple shaped pulse applied, there would be chances that the brightness difference of the spots could be reversed, since the shaping is randomly applied. **(C)** Uncertainty on both the brightness and the position accuracy would be effectively minimized simultaneously in this summing process. More shaped pulses, six, eight, or ten, could be better for this purpose. We present further demonstration in our Supplementary Materials Fig.S6.
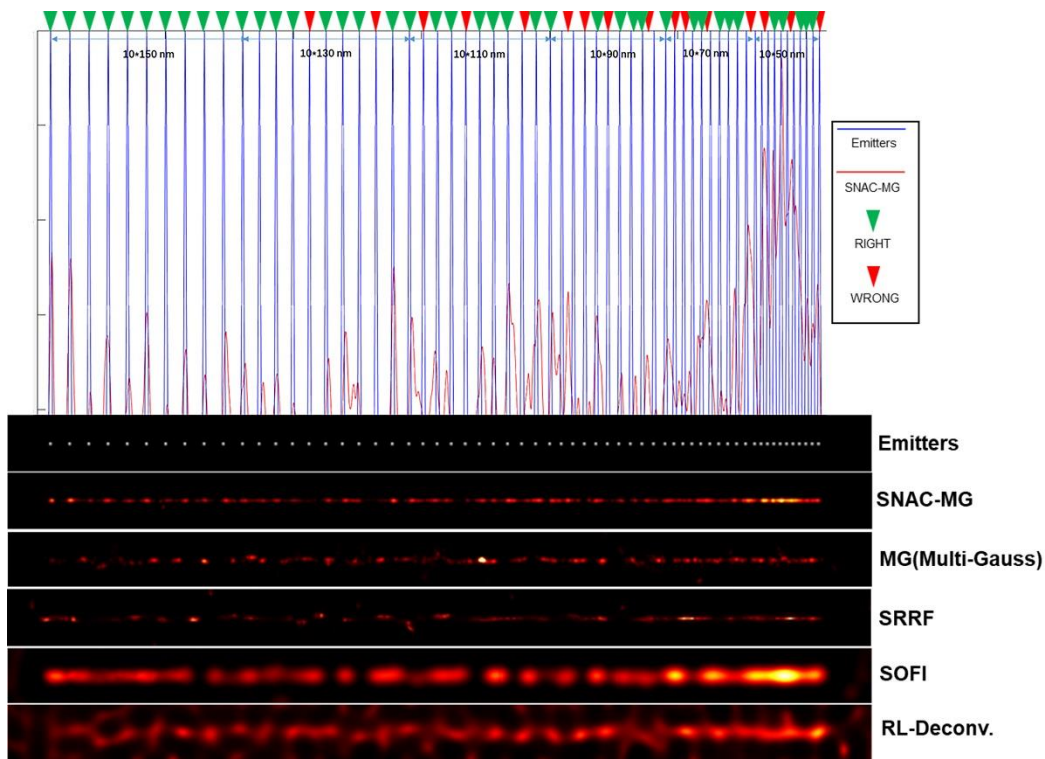
Fig. S4. Continuous asymptote reconstruction. Super-resolution is often difficult resolving for high dense probes. For continuous asymptote emitters separated 50-150nm, SNAC-MG, MG, SRRF, SOFI, RL-Deconvolution methods show reconstruction results in Fig S4. The SNAC method is the best at analytical results to straight lines. For emitters at distance above 90nm, its localization ensures a very high accuracy (green arrow). Some errors can be found for higher emitter density, while the line profile is kept with high accuracy. Since our SNAC process is a combination FFT for periodic data, the variation information is extracted and then sent to the Multi-Gaussian fitting algorithm to obtain the processing result. Therefore, we directly input the raw data which has not been processed into the Multi-Gaussian fitting (MG) algorithm for comparison. It is a deterministic proof showing the power of SNAC.
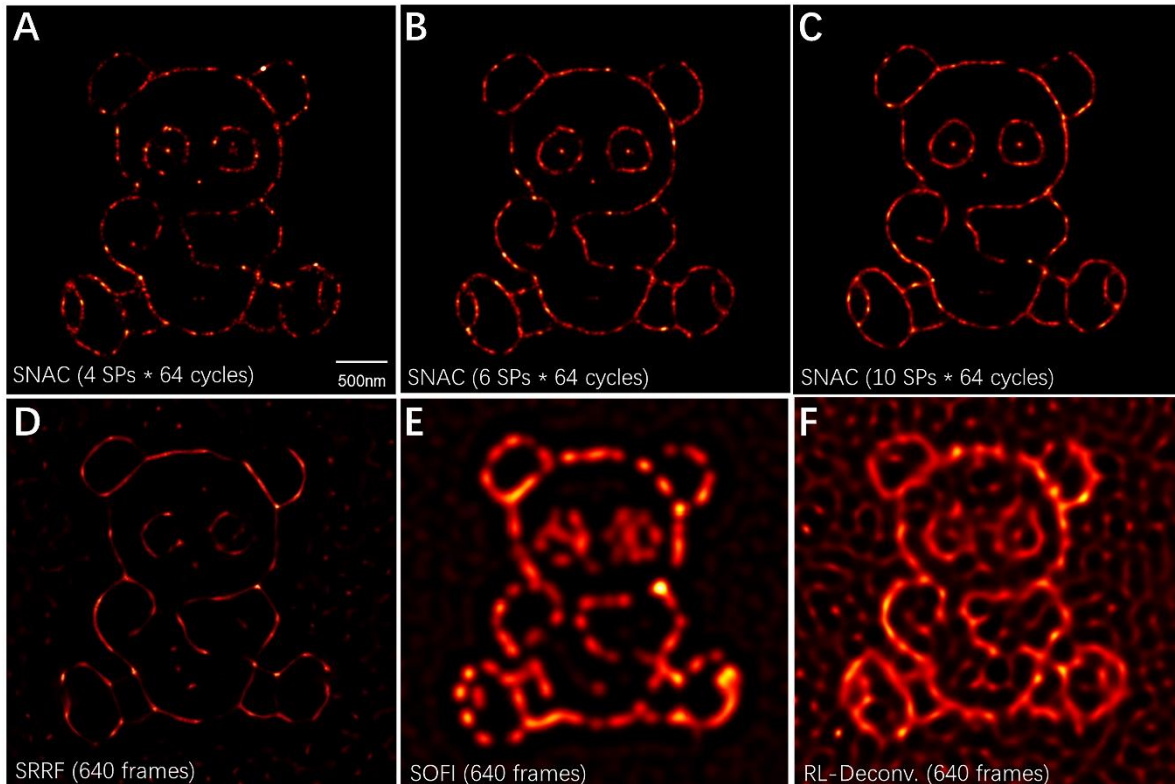
Fig. S5. The Panda reconstruction of a complex 2D-structure. The Panda is used to verify the resolution ability of the algorithm for high density continuous structures. It contains points nearest to 40nm, continuous uneven lines, complex intersecting regions, circular circles with hollow centers, and hollow ones (shown in Fig. 4**A**). Super resolution algorithms can display many common analytic scenes here. **(A)-(C)** The contour and position of the SNAC-MG results (**A**, 4 SPs in a period for 64 cycles. **B**, 6 SPs in a period for 64 cycles. **C**, 10 SPs in a period for 64 cycles.), which guides the consideration of the balance between the acquisition time and accuracy of the experimental parameters. **(D)-(F)** The analytical results of SRRF, SOFI and RL-Deconvolution algorithms for the full view of the panda structure.
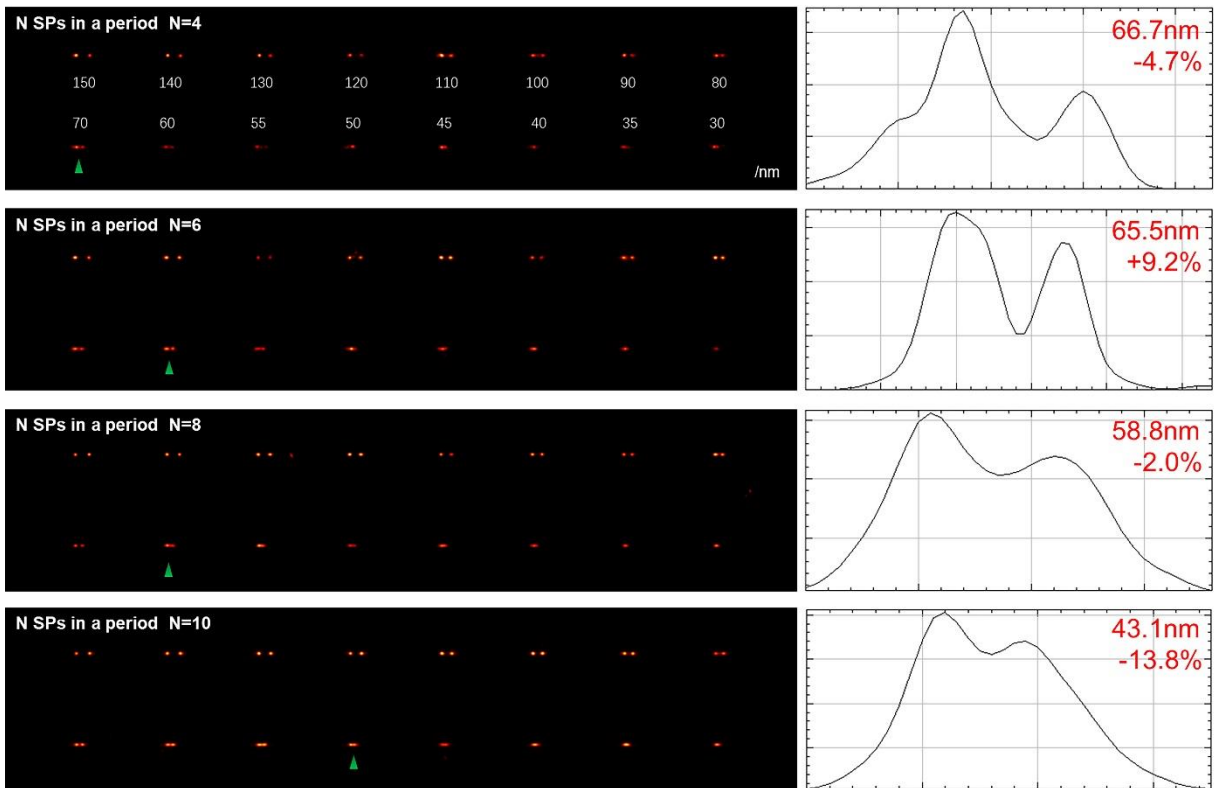
Fig. S6. Adjacent two points reconstruction and periodic N SPs effect. SNAC-MG is a method based on point resolution that extracts the brightness variation information in the cycle by actively controlling the independent response of the particles. To verify that more information can bring higher resolution, we adjust the N SPs within the period for simulation analysis (64 cycles). The figure shows the adjacent points results from 30 to 150nm by SNAC-MG when N=4,6,8,10. With the increase of the period, the uncertainty of location also decreases, and the super-resolution accuracy increases from 70 (N=4) to 50nm (N=10).
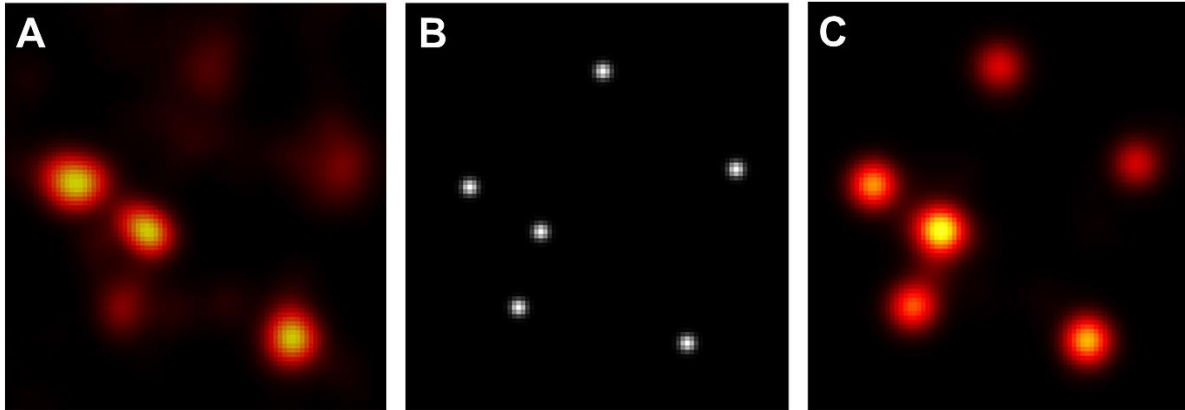
Fig. S7. Verification of super resolution capability for quantum dots. **(A)** The super-resolution results obtained from PMMA-QD thin film experiments employing SNAC algorithm. **(B)** The initial emitters' positions in **A**. **(C)** Relocation of these emitters in **B**. In order to verify the validity of the analytical capability under experimental conditions, we reset the analytical results in **A** to the initial emitters' positions in **B** for simulation, and then relocate these emitters with SNAC as showed in **C**. The approximate results between **A** and **C** confirm the validity of the SNAC in the analysis of experimental data.
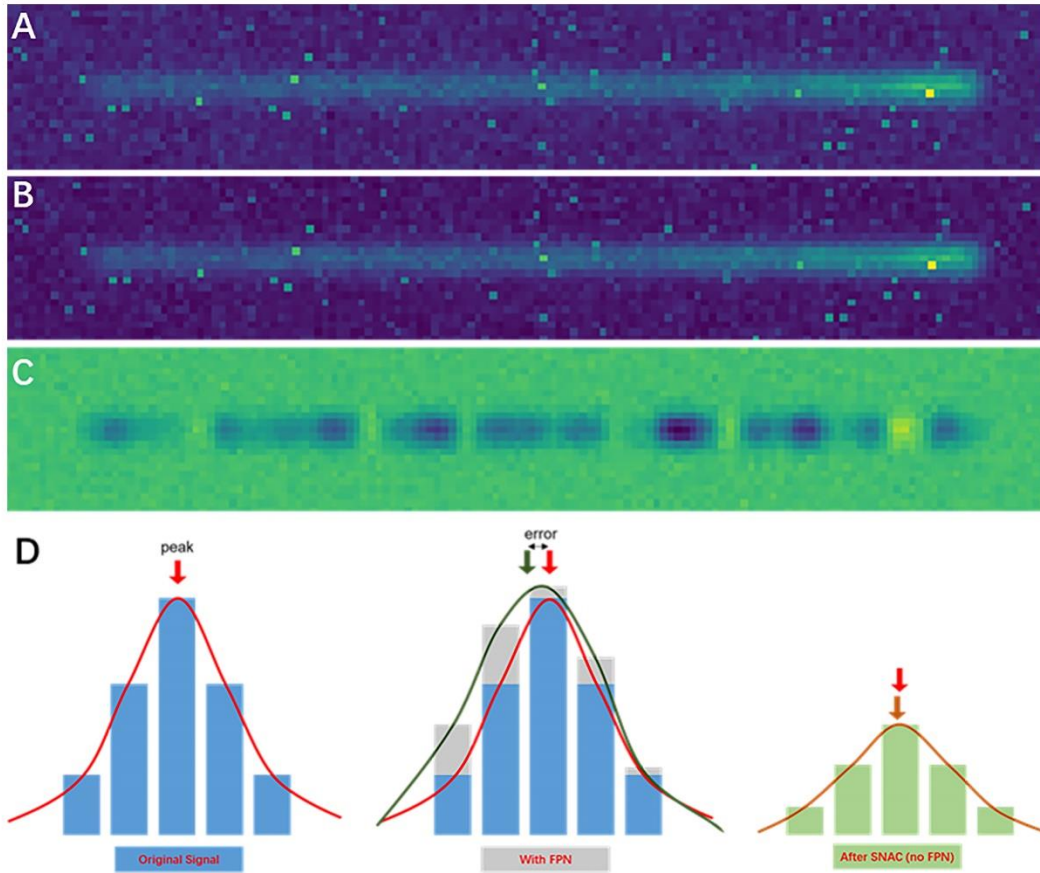
Fig. S8. The contrast of noise reduction between convention and FFT extraction. Super-resolution reconstruction is essentially a fitting process, so the impact of noise on the quality of the fit is critical. In sCMOS imaging acquisition, there are often two main types of noise, one is random Poisson noise, and the other is fixed pattern noise (FPN) due to electronic processes. When processing data, random noise can usually be eliminated by de-biasing, while FPN has a strong impact on signal destruction. **(A)** The original image with noises for an asymptote line. **(B)** The noise reduction processing by de-biasing method for original image. **(C)** SNAC uses the FFT to extract the periodic variation, eliminating a lot of noise that is inconsistent with the period. **(D)** The figure below demonstrates the effect of FPN on the deviation of the fitting results and the improved accuracy of the SNAC after removing the effects of FPN.

| Methods	Lateral resolution(nm)	Integration time	Acquisition frames	Sample requirements	Shortcoming
Confocal	200-250	ms-s	-	Broad	Low-resolution
(F)PALM/STORM	10-40	s-min	100-1000	Sparse photoswitchable fluorophores	Long acquisition time; Difficulties in sample preparation
STED	20-70	ms-s	1000-10000	Photostable fluorophores	Phototoxicity; High-cost
SPoD/SDOM	~130	ms-s	10-20	Dipolar fluorophores	Low-resolution; High density inapplicability
SOFI	~100	ms-s	1000-2000	Blinking QDs	Low-resolution; Poor selectivity of sample
JT-SOFI	~85	ms-s	100	Blinking/switching fluorophores	Low-resolution; Poor selectivity of sample
(S)SIM	~100,(S)50	ms-s	600	Strong and stable fluorophores	Saturating radiation damage; High-cost
SNAC	30-50	ms-s	100-1000	Almost broad	High density inapplicability
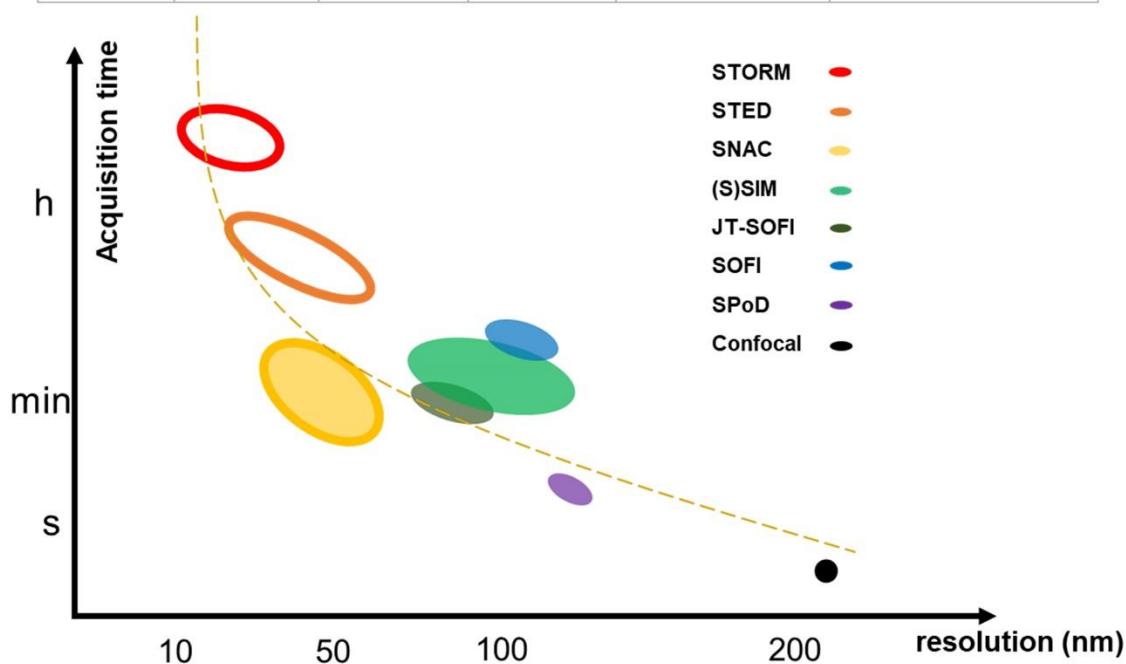
Fig. S9. Summary and comparison of mainstream super-resolution microscopy techniques. Summary table and comparison of mainstream super-resolution microscopy techniques including Confocal, SOFI, JT-SOFI, STORM, STED and (S)SIM and SNAC (yellow outline marked).
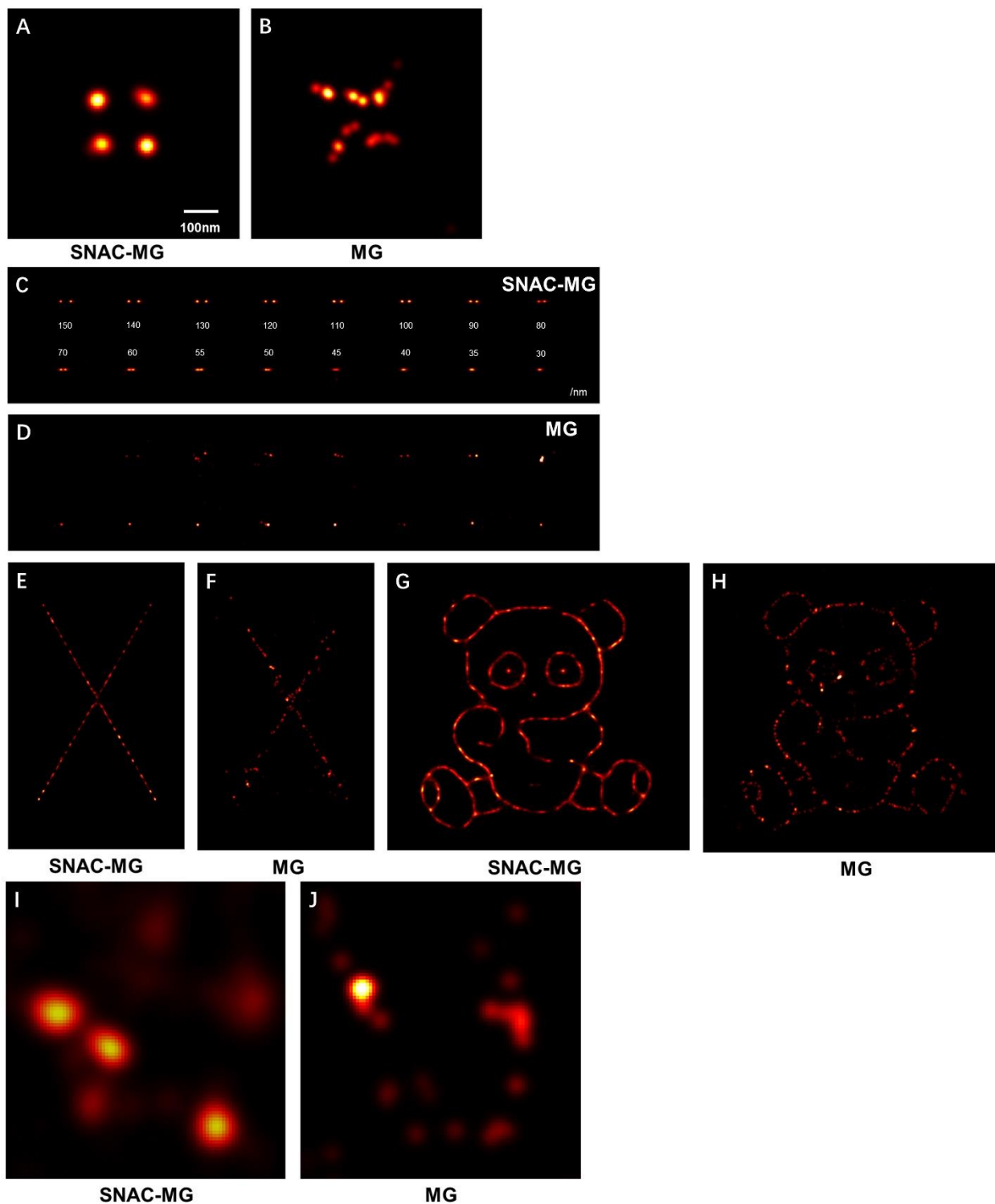
Fig. S10. Multi-Gaussian fitting on averaged image for comparation. For confirming the effect of SNAC method, the multi-Gaussian fittings are applied to SNAC image series and to images averaged to all images within a period. The results shows SNAC image series contain critical information for achieving final super-resolution.